Separation and Purification Technology 389 (2026) 136767

Contents lists available at ScienceDirect

Separation and Purification Technology

journal homepage: www.elsevier.com/locate/seppur

Droplet motion and detachment of individual oil droplets on a horizontally mounted oleophobic fiber under transverse gas flow

Alexander Schwarzwälder *, Jörg Meyer, Achim Dittler

Karlsruhe Institute of Technology, Institute of Mechanical Process Engineering and Mechanics, Straße am Forum 8, Karlsruhe, 76131, Baden-Württemberg, Deutschland, Germany

ARTICLE INFO

Communicated by Volodymyr Tarabara

Keywords:
Droplet–fiber interaction
Droplet detachment from fiber

ABSTRACT

The interaction of liquid droplets with fibers is a key phenomenon in many technical applications, especially in coalescence filtration. While previous studies have addressed droplet detachment under various gas flow conditions and fiber surface properties, detailed experiments capturing the full dynamics of crossflow-induced detachment at high temporal resolution, particularly for oleophobic fibers, remain limited. In this study, we investigate the motion and detachment of individual oil droplets on a horizontally mounted, oleophobic stainless steel fiber exposed to transverse air flow at filtration-relevant velocities as low as $1.3\,\mathrm{m\,s^{-1}}$, representative of locally elevated velocities within fibrous filter media. Using high-speed imaging at up to 42 345 fps, we resolve the droplet dynamics, including oscillation, deformation, and necking on millisecond time scales. The individual droplets of a standard compressor oil with volume-equivalent sphere radii between $276\,\mu\mathrm{m}$–$749\,\mu\mathrm{m}$ were placed on a single oleophobic fiber with a diameter of $80\,\mu\mathrm{m}$.

The experiments are conducted in a viscous-inertial regime characterized by moderate Weber numbers (We ≈ 3–5) and relatively high Ohnesorge numbers (Oh ≈ 0.5–1). The results reveal high-frequency oscillations up to 160 Hz for small droplets ($r_d = 276\,\mu\mathrm{m}$) and show that droplet detachment proceeds via ligament elongation and pinch-off, forming only a few satellite droplets. For oleophobic fibers, the droplets adopt a clamshell-shaped configuration in axial view, whose blow-off dynamics are resolved here for the first time at high temporal resolution.

1. Introduction

The interaction of liquid droplets with solid surfaces in a surrounding gas phase is a fundamental phenomenon in fluid mechanics and materials science. It plays a crucial role in numerous engineering applications, including coating processes and coalescence filtration, and is particularly relevant to oil-mist separation [1].

Previous studies have investigated various aspects of the droplet–fiber interaction, including contact angles and wetting behavior [2–4], droplet transport along fibers [5], droplet impact [6], as well as coalescence, growth, and detachment [7–10]. Influencing parameters such as surface roughness, contact angle hysteresis, fiber orientation, external fields, and fluid properties have also been extensively studied [3,11–13].

The droplet detachment from fibers is a highly dynamic process, governed by a complex interplay of forces acting at the solid–liquid–air interface. Although droplet–fiber interactions have been widely studied, detailed experiments capturing the highly dynamic detachment process at millisecond time scales are still lacking, which provides the motivation for the present study.

A number of studies have shown that, in technical coalescence filtration, droplets typically grow to sizes of several hundred micrometers to millimeters on single fibers, while local gas velocities in the pore space of fibrous filters reach several meters per second [1]. These operating conditions generally lead to droplet-scale Weber numbers of order unity, meaning that aerodynamic and capillary forces are of comparable magnitude. The present experiments, conducted with compressor oil droplets of radii between $276\,\mu\mathrm{m}$–$749\,\mu\mathrm{m}$ and gas velocities up to $15.9\,\mathrm{m\,s^{-1}}$, fall into a Weber-number regime of $3.2 \leq \mathrm{We} \leq 5.2$. These values represent not an exotic high-Weber condition but rather the upper envelope of practically relevant droplet–fiber interactions in coalescence filtration systems.

In the following section, the most relevant literature concerning droplet detachment from fibers in a 3-phase solid–liquid–gas system will be summarized.

---

* Corresponding author.
E-mail address: alexander.schwarzwaelder@kit.edu (A. Schwarzwälder).

https://doi.org/10.1016/j.seppur.2026.136767
Received 3 November 2025; Received in revised form 18 December 2025; Accepted 2 January 2026

The behavior of water droplets on vertically mounted fibers under the influence of both gravitational and aerodynamic forces has been extensively studied in the context of liquid aerosol filtration by Mullins et al. [14,15] for the droplet morphology of clamshell-shaped and barrel-shaped droplets.

The studies focused on the mechanisms of droplet motion, oscillation, and detachment as a function of increasing air velocity, particularly in the transitional Reynolds number regime. Water droplets were generated via aerosol coalescence and deposited onto the fibers, where their growth, displacement, and removal were analyzed using cameras with a frame rate of 25 fps–80 fps. Stainless steel fibers with a diameter of 28 μm were used for clamshell droplets [14], while barrel droplets were investigated on thinner glass fibers with a diameter of 7.1 μm [15]. The corresponding droplet radii ranged from approximately 100 μm to 250 μm for clamshell droplets, and from 50 μm to 160 μm for barrel droplets.

A key finding in both studies [14,15] was the onset of droplet oscillation prior to detachment. These oscillations emerged at Reynolds numbers around $\mathrm{Re} \approx 100$ and were attributed to the transition from laminar to unsteady or turbulent flow around the droplet. Oscillation was characterized by the radial and angular displacement of the droplet area centroid, driven by fluctuating aerodynamic drag forces and counteracted by capillary tension.

The frequencies of the observed oscillations revealed a dominant low-frequency component in the range of 2 Hz–8 Hz, depending on droplet size and airflow velocity. In the case of clamshell droplets, the primary radial oscillation frequency was approximately 2.1 Hz, while barrel droplets exhibited slightly higher values around 6 Hz. Additionally, both droplet types showed evidence of higher-frequency modes (up to 20 Hz–35 Hz), which were interpreted as harmonics or flow-induced perturbations in the wake. These multiple frequency components suggest a nonlinear response of the droplet system and indicate the presence of complex fluid–structure interactions within the transitional flow regime.

For clamshell droplets, the downstream displacement r of the droplet area centroid prior to oscillation followed a nonlinear trend with Reynolds number:

$$r = 1.18 \times 10^{-7} \cdot \mathrm{Re}^{3.91}, \tag{1}$$

whereas for barrel droplets, the relationship was approximately linear:

$$r = 0.235 \cdot \mathrm{Re}. \tag{2}$$

While Mullins et al. [14,15] focused on the behavior of water droplets on vertically mounted fibers under realistic filtration conditions, other studies have investigated droplet detachment under idealized or more controlled settings. For example, Hotz et al. [16], Sahu et al. [10], Ojaghlou et al. [17], and Amrei et al. [8] examined the motion and detachment of defined individual droplets on single fibers.

A comprehensive experimental study on droplet detachment from cylindrical fibers was conducted by Hotz et al. [16], who investigated the influence of fiber wettability and droplet–fiber geometry on the required detachment force induced by a gas flow. Using an atomic force microscope, they measured the force necessary to remove individual oil droplets from oleophilic and oleophobic fibers, as well as from intersecting fibers and fiber mats. The results showed that the detachment force increases with fiber diameter and is significantly higher for oleophilic surfaces, which support axisymmetric (barrel-like) droplet morphologies. In contrast, oleophobic fibers exhibited clamshell-shaped droplets with lower detachment forces. When droplets were attached to two intersecting fibers, the required force increased, but by less than a factor of two due to geometric redistribution of contact forces.

To describe these effects, the authors developed a theoretical and empirical model based on the effective contact line length L_p. The normalized detachment force F scaled as a power law with

$$\left(\frac{F}{\sigma}\right)_{\text{philic}} = 1050 \cdot l_p^{0.47}, \tag{3}$$

$$\left(\frac{F}{\sigma}\right)_{\text{phobic}} = 223 \cdot l_p^{0.37}, \tag{4}$$

where σ is the surface tension and l_p is the effective contact length in meters. These correlations capture the key dependencies of the detachment force on fiber–droplet configuration and are applicable across a wide range of fiber diameters and surface properties. The study complements previous droplet dynamics work under flow conditions [14,15].

A systematic investigation of the various detachment and breakup modes of droplets from thin fibers exposed to air flow perpendicular to the fiber axis was conducted by Sahu et al. [10]. To identify the breakup modes, silicone oil droplets with different viscosities in the range of 10 mPa s–100 mPa s were deposited on hydrophilic fused silica fibers with a diameter of 90 μm. The air velocities ranged from 7.2 m s^{-1}–22.7 m s^{-1}, corresponding to Weber numbers between approximately 2 and 40. The motion and deformation of the droplets were recorded using high-speed cameras operating at frame rates up to 3500 fps.

Breakup mechanisms observed include vibrational modes at moderate Weber numbers, in which the droplet begins to oscillate due to aerodynamic excitation and detaches in a stamen-like manner. At higher Weber numbers, the mode called bag breakup dominates, which describes the inflation of the droplet similar to a bag caused by the flow. The droplet inflates into a thin membrane that ruptures under aerodynamic pressure. A transitional regime, referred to as bag-and-stamen breakup, was also observed, where a central liquid filament temporarily connects the droplet to the fiber before breaking.

A key outcome of the study is the definition of two critical Weber numbers: a lower threshold at $\mathrm{We} \approx 2$, marking the onset of detachment, and an upper threshold beyond We 40–50, associated with the onset of complete aerodynamic breakup.

Sahu et al. [10] provided a detailed experimental classification of breakup modes under aerodynamic forces. The underlying force balance and scaling behavior at the microscopic level have been further explored in numerical studies [17].

Ojaghlou et al. [17] conducted molecular dynamics simulations to investigate the detachment force required to radially remove a water droplet from a smooth, hydrophilic fiber. Additionally, the residual liquid volume remaining on the fiber after detachment was determined. Their results demonstrate that the minimum force per liquid molecule increases as the droplet volume decreases, following a characteristic scaling law of $F_{min} \propto V_r^{-2/3}$. The simulation results are in good agreement with experimental findings reported by Amrei et al. [8] and with continuum-level simulations of macroscopic droplets performed using the Surface Evolver code [8].

A key observation in the work of Ojaghlou et al. [17] is the dependence of the residual volume on the initial droplet size. As the droplet volume increases, the absolute amount of residual liquid left behind on the fiber after detachment also increases. However, the relative residue, the fraction of the initial droplet volume that remains, decreases with droplet size.

By analyzing the breakup profile of detaching droplets, the authors showed that the maximum residual volume scales sub-linearly with droplet size, approximately $V_{res} \propto V^{2/3}$

Aziz et al. [18] demonstrated that the droplet residue volume is most strongly influenced by the fiber wettability and fiber diameter, while the effects of droplet size and fluid viscosity appear to be less significant within the investigated parameter range. Hydrophobic and thin fibers promote minimal liquid residue upon detachment.

In an effort to develop a generalized model for the droplet detachment force from cylindrical fibers, Farhan and Tafreshi [19] conducted a combined experimental and numerical study that accounts for the effects of droplet geometry, surface wettability, and fiber curvature. Their work aims to provide a predictive framework for the normal detachment force required to remove a droplet from a fiber, regardless of the specific detachment mechanism involved (e.g., gravitational, magnetic, or aerodynamic).

The study utilized ferrofluid droplets subjected to magnetic fields to measure the detachment force in a controlled and repeatable manner. These experiments were complemented by simulations using the Surface Evolver software, which calculates energy-minimized droplet shapes and associated forces based on interfacial tension, volume, and contact angle constraints. The model assumes axisymmetric barrel-shaped droplets and smooth cylindrical fibers.

The authors show that the detachment force can be expressed as the balance between capillary adhesion and internal pressure forces. Two key expressions were derived from this balance. The first, a geometry-based expression, accounts for detailed droplet shape characteristics and is given by

$$F_z = \gamma l_e \sin\theta_{\text{avg}} - \frac{A_e}{2r}(r_f + 0.5 l_a),$$

where l_e and A_e are the effective contact line length and area, θ_{avg} is the average contact angle, r_f is the fiber radius, l_a is the axial contact length, and r the displacement of the droplet. The second expression is a simplified empirical approximation based solely on the maximum droplet diameter D_d and contact angle:

$$F_z = 2\gamma D_d (1 + \cos\theta_{\text{avg}}),$$

which offers a practical alternative when precise droplet geometry is not available.

To generalize the model for a wide range of conditions, the authors introduce a dimensionless scaling law that collapses all their simulation data onto a master curve:

$$F_z = \left(\frac{r_{\text{ref}}}{r_f}\right)^2 \cdot \frac{1 + \cos\theta}{1 + \cos\theta_{\text{ref}}} \cdot u \cdot V^n,$$

with $u = 3894$, $n = -0.84$, and V the droplet volume normalized by r_f^3. This correlation is valid for Young–Laplace contact angles greater than 20°. The model captures the influence of both geometric and surface-wetting parameters across a wide range of droplet sizes and fiber diameters.

Furthermore, the simulations reveal that more hydrophilic fibers (smaller contact angles) result in significantly higher detachment forces and leave behind a liquid residue upon separation. In contrast, for hydrophobic surfaces with $\theta > 100°$, droplets tend to detach cleanly without residue.

In summary, the studies known to the author provide a comprehensive overview of various aspects of droplet–fiber interaction. However, to the best of the author's knowledge, experimental investigations that examine the dynamic detachment process with high temporal resolution are still lacking.

The present work investigates individual oil droplets of defined volume, which are placed on a horizontally mounted oleophobic fiber under the influence of a transverse gas flow with high temporal resolution. The objective is to identify the resulting droplet dynamics.

2. Materials and methods

2.1. Experimental setup

Fig. 1 illustrates a schematic of the test rig. The fiber is mounted horizontally. Both ends of the fiber are rigidly embedded in transparent epoxy resin (details see Section 2.1.3). An oil droplet is positioned onto the stationary fiber using a piezoelectric nozzle, which is positioned in the *xyz* -directions by motorized linear stages. The droplet–fiber assembly is then exposed to a crossflow of dry air, emerging from a circular tube of diameter 20 mm. The tube has an inlet length of 1200 mm to ensure fully developed flow. The fiber is positioned 10 mm downstream of the nozzle exit, within the potential core of the jet.

Using a high-speed camera (i-speed 721, iX Cameras) paired with a macro zoom lens (12x zoom lens, Navitar) in combination with back-lighting, the droplet and fiber contours are captured at a high temporal resolution of 42 345 fps. All experiments are conducted at ambient pressure. The measured temperature at the position of the fiber is 23 °C.

2.1.1. Velocity profile of the free stream

The fiber is exposed to a crossflow emerging from a cylindrical nozzle. The volumetric flow rate of particle-free air is controlled using a mass flow controller (SLA5853, Brooks Instrument GmbH) and can be adjusted within a range of $20\,\mathrm{N\,L\,min^{-1}}$–$220\,\mathrm{N\,L\,min^{-1}}$. The absolute velocity was measured for several flow rates with a hot-wire anemometer (CTV 210-BOS-R, KIMO Instruments) at the fiber position (without the fiber installed), as shown in Fig. 2. The white region, marked with the letter A, indicates the field of view observed in the experiments along the vertical y-direction, where $y = 0$ corresponds to the centerline of the gas outlet. It can be seen that within this region, the velocity profile can, to a good approximation, be considered constant.

From the velocity profiles, an average flow velocity $\bar{u}$ within the field of view is obtained, which can be approximated as a linear function of the volumetric flow rate: $\bar{u} = 0.069\,\mathrm{L/min} \cdot \dot{V}$ (see Fig. 3).

2.1.2. Properties of the liquid of the droplet

A standard compressor oil is used as the working fluid (Rotor Inject Fluid Ndurance, Atlas Copco Airpower nv.).

The dynamic viscosity, measured with a shear-rate-controlled rheometer at a shear rate of $10\,\mathrm{s^{-1}}$ in the temperature range of 20 °C–40 °C is shown in Fig. 4 (left y-axis). It can be observed that the dynamic viscosity of the compressor oil decreases continuously with increasing oil temperature.

The surface tension was experimentally determined on a pendant drop in air using an optical contact angle measuring device with a contour analysis system (OCA, DataPhysics Instruments GmbH), equipped with a dosing needle of 1.83 mm outer diameter. The measurement was conducted at three temperatures of 22 °C, 27 °C and 32 °C over a period of 10 min, during which the average drop volume was $13.75 \pm 2.23\,\mathrm{\mu L}$. For each temperature, three measurements were performed. According to Fig. 4 (right y-axis), no significant temperature dependence of the surface tension was observed. The averaged mean surface tension was $31.94 \pm 0.22\,\mathrm{mN\,m^{-1}}$.

The density of the oil, determined at 20 °C using an oscillating U-tube densitometer (Densito 30PX, Mettler-Toledo International Inc.), was found to be $870\,\mathrm{kg\,m^{-3}}$, which is in agreement with the manufacturer's specification.

2.1.3. Clamping device, fiber and coating

The clamping device allows the fiber to be securely clamped on both sides within transparent resin blocks (see Fig. 5). Epoxy resin is applied on each side, sandwiched between two transparent PMMA plates positioned within a 3D printed PLA structure. The fiber is clamped with a tensile force of 2.45 N.

The fiber used in this study has a nominal diameter of 80 μm. The fiber core is composed of stainless steel and was supplied by Carl Haas GmbH. An oleophobic coating known as ProSurf, developed by Surfactis Technologies, was applied using a repeated dip-coating process. The coating consists of perfluoropolyether compound dissolved in a fluorinated solvent. Although the manufacturer does not disclose the detailed chemical formulation, the coating belongs to the class of fluorinated amphiphilic monolayers that lower the surface free energy through densely packed CF_2/CF_3 end groups.

SEM images of uncoated and coated fibers are shown in Fig. 6 to highlight the influence of the coating on the fiber diameter. Each image represents a separately prepared fiber sample. In Fig. 6(a), the uncoated fiber has a homogeneous surface with occasional contamination and longitudinal grooves in the submicron range. These grooves are attributed to the drawing process during manufacturing. Fig. 6(b) shows a fiber coated 5 times by dipping into the coating solution and cleaned afterwards 50 times by dipping into ethanol.

No measurable increase in fiber diameter was detected after coating. A comparison of the surface morphology shows visible differences. The coated fibers exhibit numerous fine fissures and occasional larger cracks in the coating, which are assumed to result from mechanical stress

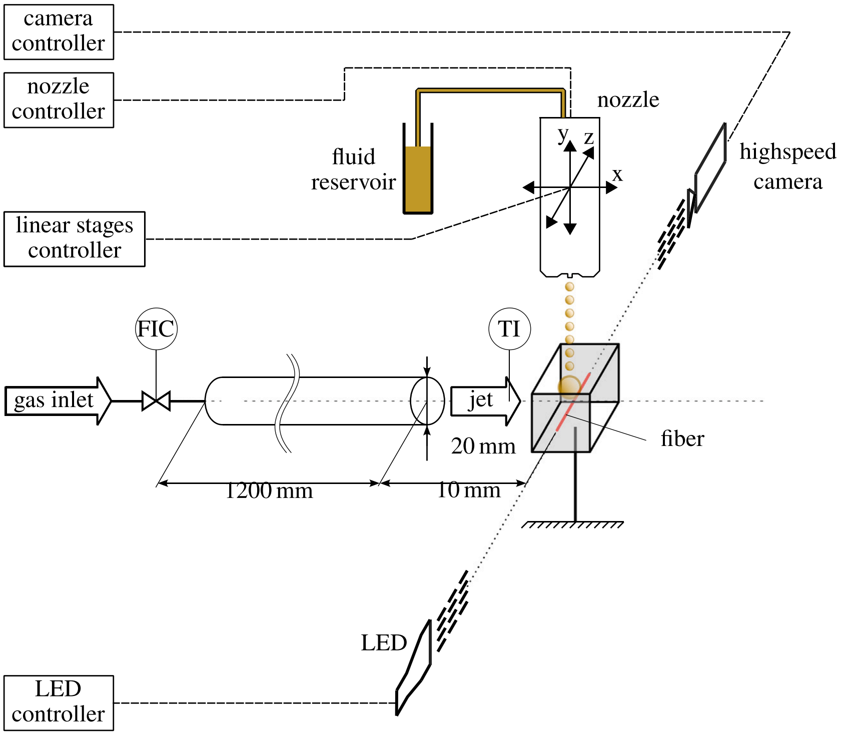

Fig. 1. Schematic diagram of the experimental setup.

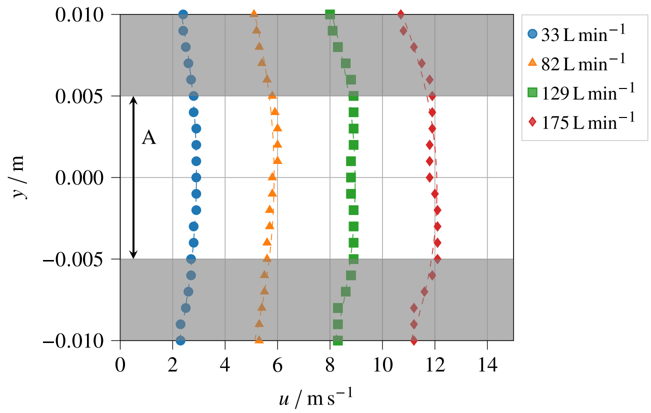

Fig. 2. Flow profiles at the fiber position obtained from separate measurements without the fiber installed. The height $A = 8\,\mathrm{mm}$ indicates the maximum field of view considered in the recordings.

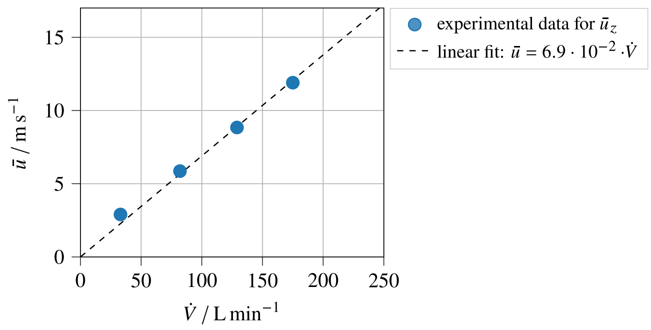

Fig. 3. Mean velocity $\bar{u}_z$ at the position of the fiber (in absence of the fiber) averaged over $y \in [-5, 5]\,\mathrm{mm}$.

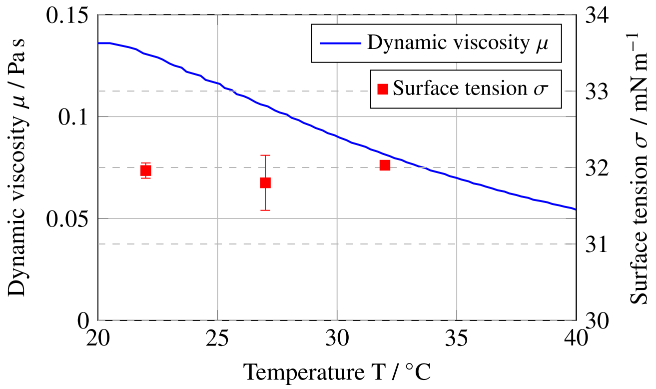

Fig. 4. Temperature dependence of the dynamic viscosity (blue) and surface tension (red) of the compressor oil.

during repeated dipping (of the one-sided fixed fiber before installing in the clamping device).

The surface roughness of the fiber was measured along five line profiles using a laser scanning microscope (VK-X100, Keyence). The arithmetic mean roughness R_a was determined to be $0.047\,\mu\mathrm{m}$.

To quantify the wetting characteristics of the coated fiber, advancing, receding, and static contact angles were determined in preliminary experiments published in a previous work [20]. The droplet contour near the triple line was approximated by polynomial fitting, and the tangent at the contact point was used to compute the local contact angles. Averaging over eight measurements yielded an advancing angle of $\theta_{\mathrm{adv}} = 111° \pm 7°$, a receding angle of $\theta_{\mathrm{rec}} = 76° \pm 12°$, and a static contact angle of approximately $\theta_{\mathrm{eq}} = 90° \pm 9°$. These values confirm that the coating produces an oleophobic surface with a moderate contact angle hysteresis.

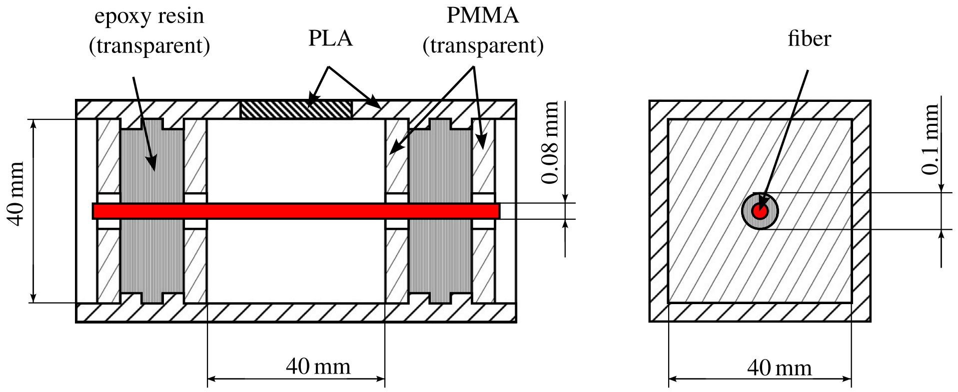

(a) Radial view of clamping device

(b) Axial view of clamping device

Fig. 5. Schematic sketch of clamping device [20].

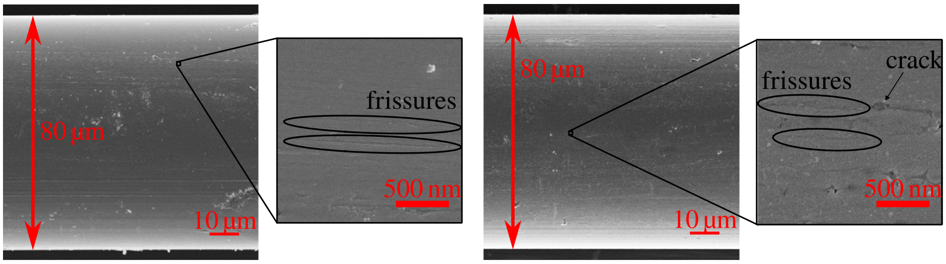

(a) Uncoated fiber

(b) 5× coated, 50× cleaned by dipping in ethanol

Fig. 6. SEM Images with a comparison of the untreated and coated stainless steel fiber.

2.1.4. *Camera setup and spacial resolution*

The high-speed camera (i-Speed 721, iX Cameras) was equipped with a modular macro lens (12× zoom lens, Navitar) in combination with an extension tube (length = 100 mm). The optical resolution of this camera setup was determined using a 1951 USAF resolution target and ranges, depending on the selected field of view, from 28.5 $\mathrm{lp\,mm^{-1}}$–128 $\mathrm{lp\,mm^{-1}}$. For the experiments, the field of view was chosen such that the deforming droplet was imaged as large as possible while ensuring that the droplet remained fully within the frame throughout the entire detachment process.

Based on the measured optical resolution, the smallest resolvable feature size Δx can be estimated from $\Delta x \approx \frac{1}{2\,(\mathrm{lp\,mm^{-1}})}$. Hence, depending on the selected field of view, the smallest resolvable feature is on the order of 4 µm–18 µm (see Fig. 7).

2.2. *Experimental procedure*

Oil is deposited onto the fiber by first releasing 10 droplets with a piezoelectric nozzle (MD-K-140, microdrop Technologies) to verify correct placement and the absence of rebound by visual inspection. A single droplet has a diameter of 74.9 µm. The procedure is then repeated with 90 additional droplets (100 in total). These two steps guarantee the formation of a sufficiently large droplet on the fiber, enabling the subsequent deposition of the remaining droplets in a single run without verifying each individual droplet placement (compare Fig. 8). The number of droplets is chosen such that the desired final droplet volume of the coalesced droplet on the fiber is achieved.

The droplet volumes deposited on the fiber in this study were 22, 44, 88, and 177 nL. Due to the downward-acting gravitational force as well as the momentum transfer of the individual droplets during coalescence with the liquid already deposited on the fiber, the coalesced droplet aligned in a hanging configuration on the fiber. The resulting initial configurations for the respective droplet volumes are shown in Fig. 9.

It can be observed that for small droplets with radii in the range of r_d = 276 µm to 594 µm, gravitational forces are not sufficient to align the droplet vertically. This deflection is attributed to the non-ideal centering of droplet deposition during the experiment as well as to surface inhomogeneities of the fiber. Adhesion and capillary forces dominate gravitational force, and the droplet remains deflected on the fiber. With increasing droplet volume, gravitational effects become more pronounced, and for r_d = 749 µm it is observed that gravity aligns the droplet vertically.

After droplet deposition and coalescence, the cross flow was switched on at an initial flow rate of 20 $\mathrm{L\,min^{-1}}$ (≃ 1.38 $\mathrm{m\,s^{-1}}$). The flow rate was then increased in increments of 20 $\mathrm{L\,min^{-1}}$. After each increment, a video of the droplet was recorded, capturing at least five periods of its oscillatory motion. The gas flow was increased until either a maximum flow rate of 230 $\mathrm{L\,min^{-1}}$ (≃ 16.56 $\mathrm{m\,s^{-1}}$) was reached or the droplet detached from the fiber.

2.3. *Post-processing of the image series to determine the motion of the droplet*

Using MATLAB, the video recordings were analyzed frame by frame. The fiber position was manually annotated. The droplet was isolated by binary segmentation and tracked across all frames using MATLAB's tracking tools. For each frame, the droplet's area centroid was computed, and the relative position between the droplet and the fiber was determined.

Satellite droplets that may form during detachment from the fiber are only a few pixels in size and therefore cannot be reliably detected automatically across all recordings. Consequently, satellite droplets were manually marked after detachment, and smaller satellite droplets might be missed.

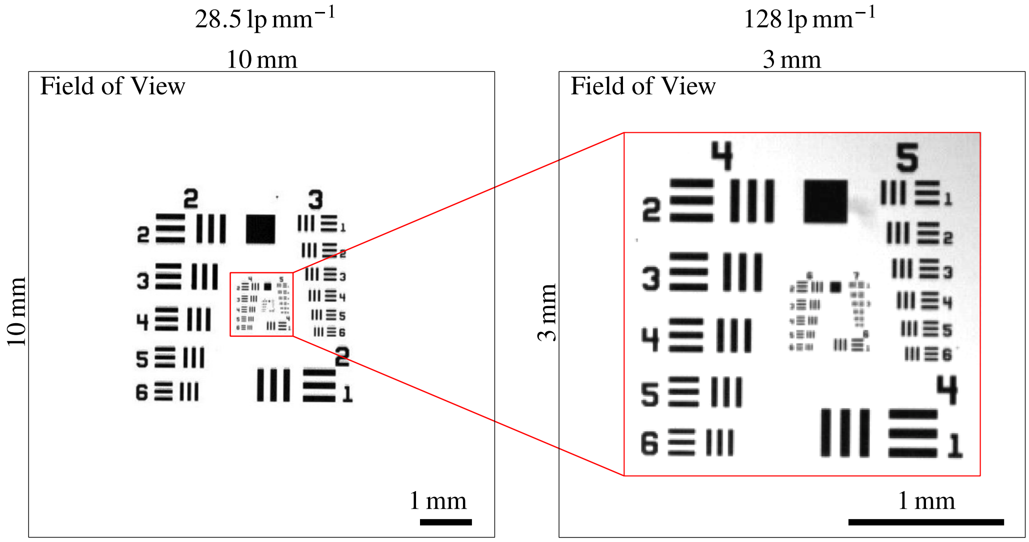

Fig. 7. Spatial resolution of the high-speed camera setup for the maximum field of view of $10 \times 10\,\mathrm{mm}$ with $28.5\,\mathrm{lp\,mm^{-1}}$ (left), and minimum field of view of $3 \times 3\,\mathrm{mm}$ with $128\,\mathrm{lp\,mm^{-1}}$ (right) based on the 1951 USAF targets.

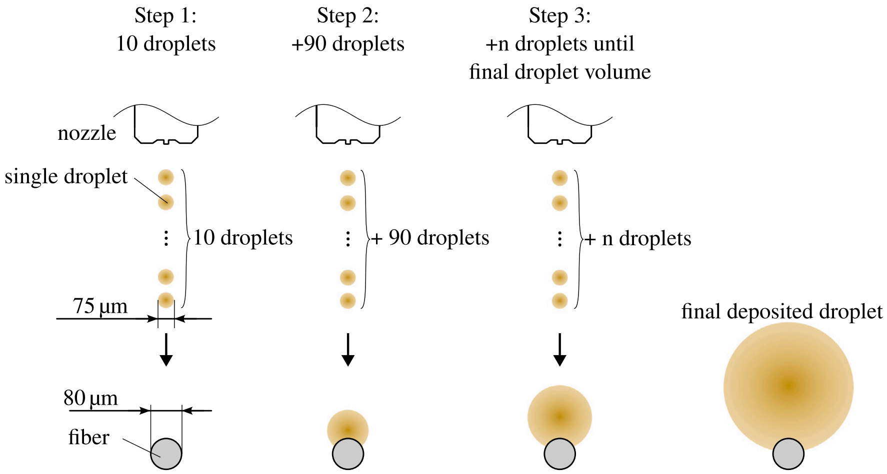

Fig. 8. Sketch of droplet deposition procedure.

3. Results

The following section analyzes the dynamics of a droplet deposited on a fiber under an imposed gas flow. First, in Section 3.1 the oscillatory motion prior to detachment is illustrated exemplarily in an image series for one experiment and afterwards analyzed in depth for all experiments. Second, the detachment conditions are examined in detail in Section 3.2.

3.1. Oscillatory motion of a droplet in a crossflow

To illustrate the droplet dynamics under crossflow, Fig. 10 shows a sequence of high-speed images, where every 47th frame of the recorded video was extracted ($\Delta t = 1.11\,\mathrm{ms}$). The droplet appears dark against a light gray, non-uniform background due to back-lighting with multiple high-power LEDs and inhomogeneities of the fiber holder. The identification of the droplet is unaffected by the light gray background. The fiber position is indicated by a red crosshair. The droplet's volume equivalent sphere radius r_d is $473\,\mathrm{\mu m}$. The mean flow velocity is constant at $\bar{u} = 11.8\,\mathrm{m\,s^{-1}}$.

It can be seen in Fig. 10 that the droplet is already deflected in the flow direction in contrast to the hanging configuration as shown for the initial droplet in Fig. 9 (at $\bar{u} = 0\,\mathrm{m\,s^{-1}}$). The deflection is caused by the gas stream. In the time frame (0–14.47 ms), the droplet remains nearly at a constant radial extension relative to the fiber axis, while oscillations cause circumferential deformations. With increasing time, the droplet stretches in the flow direction and a liquid bridge forms between the droplet and the fiber. This bridge progressively thins until pronounced necking occurs near the fiber. After about 18 ms, the bridge collapses, resulting in complete detachment.

In order to show for all conducted experiments an overview of the deflection, in Fig. 11 the time-averaged relative position of the droplet centroid with respect to the fiber $\Delta\vec{C}$ is shown, where $\Delta\vec{C} = \vec{C}_d - \vec{C}_f$, and $\vec{C}_d$ and $\vec{C}_f$ are the area center of mass of the droplet and fiber, respectively. Symbols distinguish the volume equivalent-sphere radii r_d (legend), while color encodes the mean velocity $\bar{u}$ (left color bar). The solid vertical and horizontal lines indicate the fiber center reference at $(x = 0, y = 0)$.

For each droplet size, the data point at a velocity of $0\,\mathrm{m\,s^{-1}}$ represents the relative position already displayed in Fig. 9 which was present before starting the crossflow. All average droplet positions after the start of the crossflow lie at $x > 0$, i.e. downstream of the fiber, evidencing a persistent drag-induced offset. With increasing $\bar{u}$, the streamwise offset ΔC_x increases monotonically, whereas the vertical offset ΔC_y is negative, which reflects gravitational sag, and its magnitude decreases as $\bar{u}$ increases. The time-averaged centroid positions for each droplet

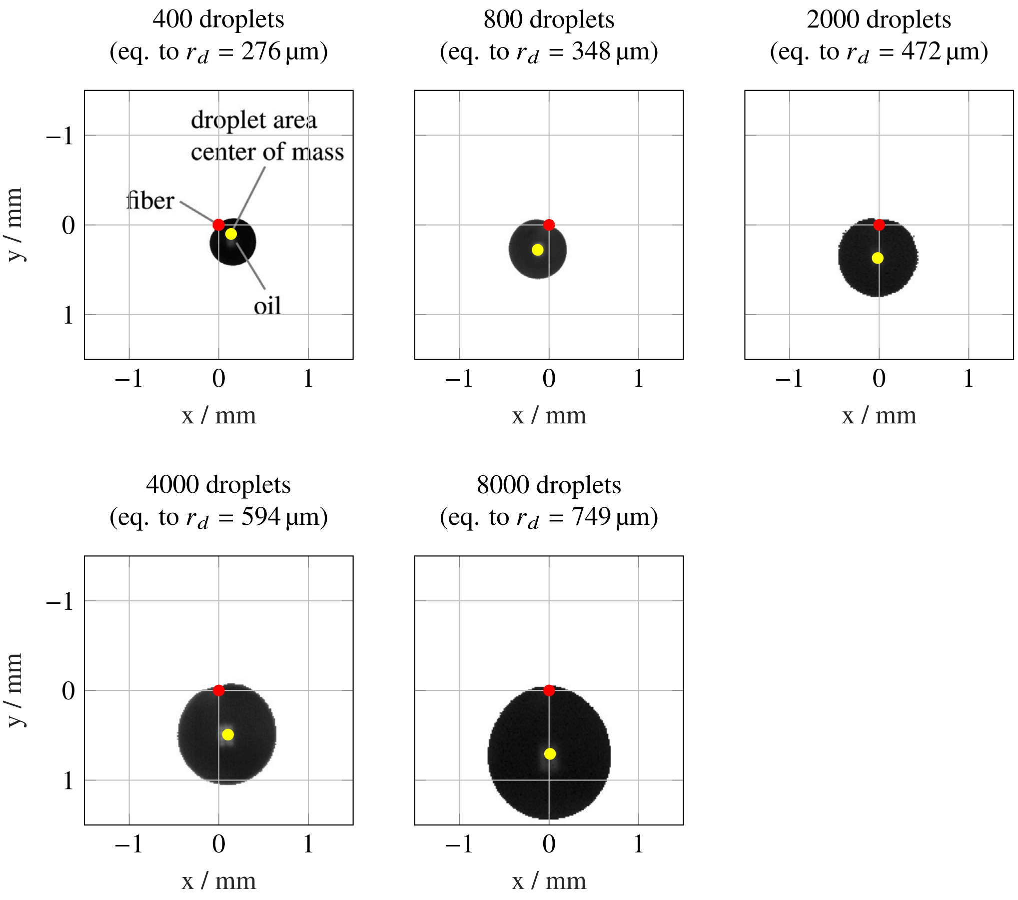

400 droplets (eq. to r_d = 276 µm)

800 droplets (eq. to r_d = 348 µm)

2000 droplets (eq. to r_d = 472 µm)

4000 droplets (eq. to r_d = 594 µm)

8000 droplets (eq. to r_d = 749 µm)

Fig. 9. Start position of the droplets without gas flow.

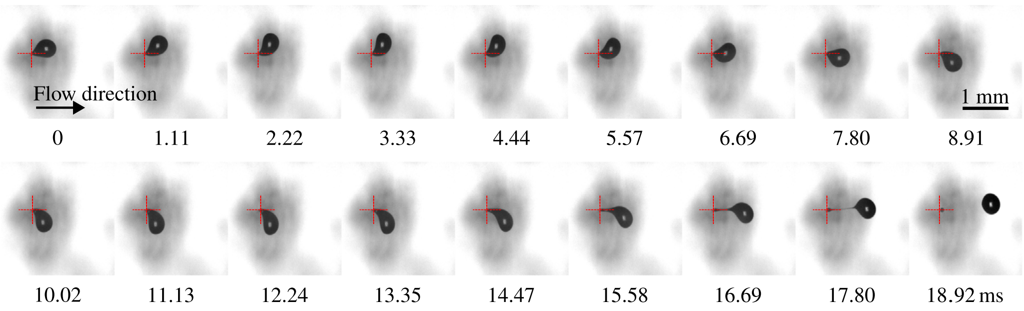

Fig. 10. Series of raw images of a droplet with $r_\mathrm{d} = 473\,\mu\mathrm{m}$ oscillating and detaching at $\bar{u} = 11.8\,\mathrm{m\,s^{-1}}$ with $\Delta t = 1.11\,\mathrm{ms}$.

size lie approximately on circles centered at the fiber. This behavior indicates circumferential advection of the droplets around the fiber at nearly constant radial distance, while the gas flow does not induce noticeable deformation under the present conditions.

The oleophobicity and hysteresis directly influence droplet adhesion behavior. A high advancing angle combined with a substantially lower receding angle leads to a finite adhesion force that stabilizes clamshell-shaped droplets on the fiber. The moderate hysteresis observed here implies that droplets can shift azimuthally under aerodynamic forcing without excessive pinning, consistent with the circumferential oscillatory motion.

As already noted, Fig. 11 shows the mean relative position for each experiment. However, the droplet is not statically fixed at a single position as the figure would suggest, but can exhibit an oscillatory motion induced by the gas flow around it. The oscillation around each mean relative position is analyzed in terms of frequency (Fig. 12) and amplitude (Fig. 14).

Fig. 12 presents the dominant frequency (marker) as a function of the flow velocity for each droplet size in every experiment, obtained from the Fast Fourier Transformation (FFT). 5000 samples (frames) were used for the time signal which was recorded at 42 345 fps. The time signal underlying the FFT describes the droplet motion in the principal motion direction. The principal direction is the direction of maximal variance of the droplet trajectory and was estimated in MATLAB using a principal component analysis (PCA).

Behind each marker, a vertical spectral line is plotted. The intensity of this spectral line reflects the amplitude of the corresponding frequency component from the FFT and was normalized to the range 0 (white) to 1 (100 % saturation of the respective marker color). The segmentation of the spectral line corresponds to the frequency resolution of the FFT, which analyzed frequencies in the range of 0 Hz–300 Hz. To avoid the overlap of spectral lines at identical flow velocities, the spectral lines were slightly offset in the plot. The tip of the horizontal

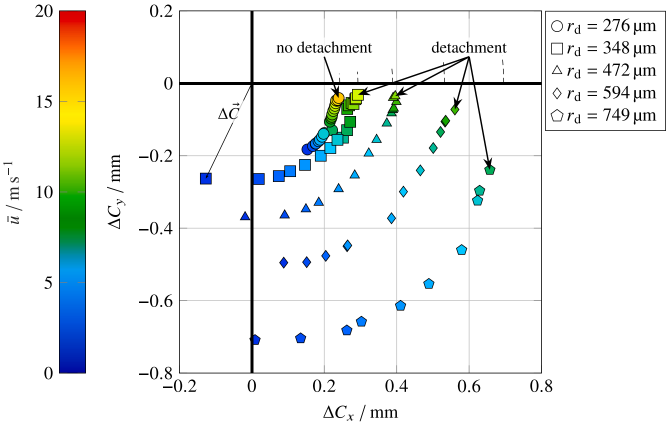

Fig. 11. Average relative position of the droplet area center of mass with respect to the fiber for each experiment $\Delta\vec{C} = \vec{C}_d - \vec{C}_f$. Symbols represent the different droplet sizes, the color the gas velocity.

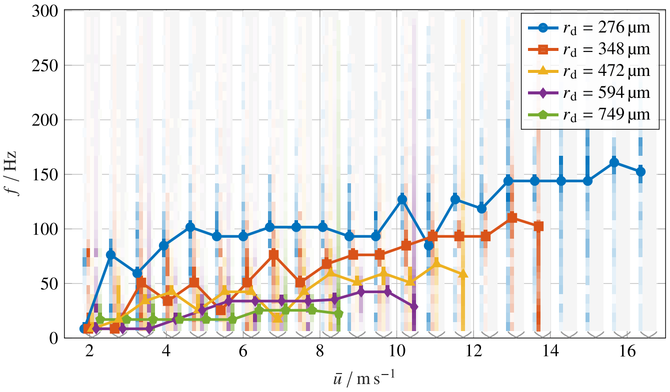

Fig. 12. Frequency in the principal direction of motion as a function of $\bar{u}$ for each investigated droplet size.

brackets on the x-axis indicate which spectral lines and data points correspond to the same velocity $\bar{u}$.

A clear trend is observed for each droplet size. The oscillation frequency increases with increasing flow velocity. At the last data point, however, the frequency decreases compared to the preceding one. This reduction is caused by the strong elongation of the droplet in the flow direction immediately prior to detachment, which leads to a decrease in oscillation frequency.

For smaller droplets, the oscillation frequencies at a given $\bar{u}$ are higher than for larger droplets. The smallest droplet ($r_d = 276\,\mu\text{m}$) reaches frequencies of about 160 Hz at $\bar{u} = 15.9\,\text{m}\,\text{s}^{-1}$, whereas the largest droplet ($r_d = 749\,\mu\text{m}$) reaches a maximum frequency of only about 25 Hz at $\bar{u} = 7.6\,\text{m}\,\text{s}^{-1}$ prior to detachment.

The measurements of the frequencies reveal oscillation frequencies of up to ~ 160 Hz, which are significantly higher than those reported by Mullins et al. [14,15]. This discrepancy can be attributed to the smaller droplet sizes investigated in the present study. The observed behavior remains qualitatively consistent with the findings of Mullins et al. [14], yet the higher temporal resolution employed here enables, for the first time, a clear characterization of the elevated oscillation frequencies exhibited by smaller droplets.

The observed decrease in oscillation frequency immediately prior to detachment can be attributed to the progressive elongation of the droplet in the direction of the gas flow. This elongation increases the effective droplet length and moment of inertia, thereby reducing the restoring capillary force that governs the eigenfrequency of the oscillatory mode. A similar frequency reduction was reported by Sahu et al. [10] for vibrating silicone oil droplets on fibers, where the transition from a nearly spherical to a ligament-like geometry causes a shift of the resonance frequency toward lower values. This "softening effect" represents the onset of capillary–inertial decoupling and marks the formation of a liquid ligament consistent with the Rayleigh–Plateau instability leading to breakup.

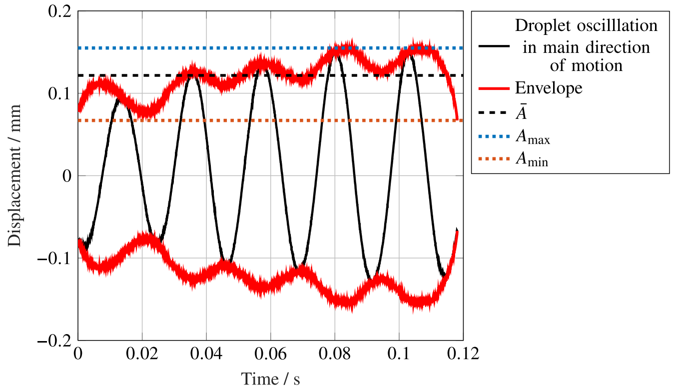

Fig. 13. Hilbert envelope for a selected experiment with $r_d = 594\,\mu\text{m}$, $\bar{u} = 9.66\,\text{m}\,\text{s}^{-1}$.

The scatter of the values in Fig. 12 is mainly due to two factors. First, the signal of the relative droplet position is limited to only 5000 frames (the maximum recorded number of frames), which leads to a broader frequency spectrum. Second, the amplitude of the relative motion in the main direction of droplet movement is only a few pixels for low flow velocities, which particularly affects the measurements at small velocities.

The amplitude of the droplet's relative motion along its principal axis is shown as a function of the mean velocity $\bar{u}$ in Fig. 14. Symbols denote the mean amplitude $\bar{A}$ of the time series for a given experiment. Vertical bars span the observed range $[A_{\min}, A_{\max}]$. The amplitudes were calculated by using the discrete Hilbert transform $\mathcal{H}\{\cdot\}$ of the scalar oscillatory time series, here being the droplet position in the principal direction of motion.

In order to determine the amplitude of a scalar oscillatory time series $s[n]$, with $n \in \{1, \dots, N\}$ indexing the samples in time, the DC component was removed by centering the signal with its sample median. This leads to

$$\tilde{s} = \text{median}\{\, s[n] \;:\; n = 1, \dots, N \,\}, \qquad s_d[n] = s[n] - \tilde{s}.$$

The discrete analytic signal $z[n]$ was then formed via the discrete Hilbert transform $\mathcal{H}\{\cdot\}$,

$$z[n] = s_d[n] + \mathrm{i}\,\mathcal{H}\{s_d\}[n], \qquad a[n] = |z[n]| = \sqrt{s_d[n]^2 + \left(\mathcal{H}\{s_d\}[n]\right)^2},$$

which defines the instantaneous amplitude envelope $a[n]$. The implementation follow the MATLAB function `hilbert` for $\mathcal{H}\{\cdot\}$.

From the envelope the following values were computed for each experiment:

$$\bar{A} = \frac{1}{N}\sum_{n=1}^{N} a[n], \qquad A_{\min} = \min_{1\le n\le N} a[n], \qquad A_{\max} = \max_{1\le n\le N} a[n].$$

The envelope and the values of $\bar{A}$, $A_{\min}$, $A_{\max}$ are shown exemplarily in Fig. 13 for the signal of the oscillatory motion of a droplet with $r_d = 594\,\mu\text{m}$ at $\bar{u} = 9.7\,\text{m}\,\text{s}^{-1}$ in its main direction of motion.

The Hilbert-transform-based envelope analysis is particularly effective when the droplet motion is dominated by a narrow-band, approximately sinusoidal oscillation. For most flow conditions considered in this study (excluding the final stages before detachment), the PCA-projected displacement signal exhibits a recognizable frequency maximum in the Fourier spectrum, while additional spectral components remain comparatively weak. Under such conditions, the analytic

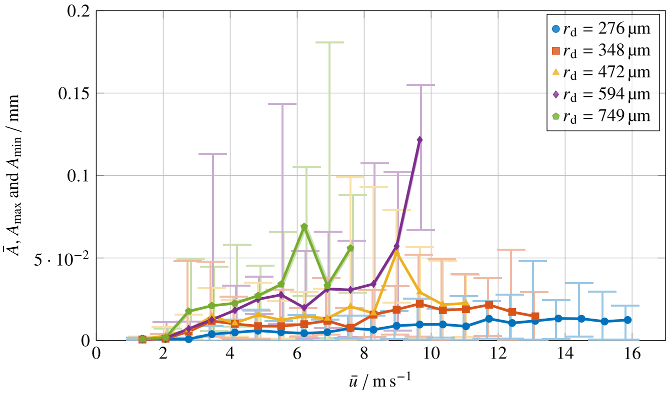

Fig. 14. Representation of mean, maximum, and minimum amplitude in the principal direction of motion as a function of the velocity $\bar{u}$.

signal provides a stable and noise-tolerant estimate of an effective instantaneous amplitude.

The method nonetheless has clear limitations. Very close to detachment, strong droplet deformation and the finite record length lead to broader spectra and additional frequency content. In this regime, the Hilbert envelope should not be interpreted as the amplitude of a single oscillatory mode but rather as an aggregate measure of the overall excursion along the principal axis. More generally, if multiple spectral components of comparable magnitude are present or if substantial frequency drifts occurs, the envelope could exhibit mode-mixing effects. At low flow velocities, the oscillation amplitude is only a few pixels, so segmentation noise and spatial quantization contribute noticeably to the scatter of $\bar{A}$ in Fig. 14.

3.2. Droplet detachment from a fiber due to cross flow

Next, the droplet-detachment process is examined in detail. Fig. 15 shows the mean velocity required to detach the droplet from the fiber as a function of r_d. The required velocity decreases with increasing r_d. For $r_d = 348\,\mu\text{m}$, the detachment velocity is $\bar{u}_{\text{det}} = 12.70 \pm 0.28\,\text{m}\,\text{s}^{-1}$. Smaller droplets could not be detached with the max. available volumetric flow rate of $16\,\text{m}\,\text{s}^{-1}$ of the compressed-air supply. At $r_d = 749\,\mu\text{m}$, the mean detachment velocity is $\bar{u}_{\text{det}} = 7.00 \pm 0.07\,\text{m}\,\text{s}^{-1}$. Additional tests, performed in the absence of a cross flow to establish the droplet volume required for purely gravity-driven detachment, were repeated 7 times. For this case, the corresponding droplet radius which detached at $u = 0\,\text{m}\,\text{s}^{-1}$ was $r_d = 929 \pm 280\,\mu\text{m}$.

The measured decrease of the detachment velocity $\bar{u}_{\text{det}}$ with increasing droplet radius r_d (Fig. 15) can be explained by a force balance that includes aerodynamic drag, capillary adhesion, and gravity. The droplet oscillates slightly in the azimuthal direction and is displaced downstream at the moment of detachment. In addition, heavier droplets sag slightly below the fiber due to gravity.

Assuming the droplet detaches when the sum of the drag force F_D and the tangential component of gravity $F_g^{\parallel}$ exceeds the capillary retention force F_σ, the detachment condition is:

$$F_D + F_g^{\parallel} \geq F_\sigma \,. \tag{5}$$

The individual contributions are approximated as follows:

- Aerodynamic drag:

$$F_D = \frac{1}{2} c_D \rho_g \bar{u}_{\text{det}}^2 A_{\text{proj}}, \quad A_{\text{proj}} \propto r_d^2 \,, \tag{6}$$

- Gravitational pull in the direction of detachment:

$$F_g^{\parallel} \sim \rho_l g V \sin\theta, \quad V \propto r_d^3 \,, \tag{7}$$

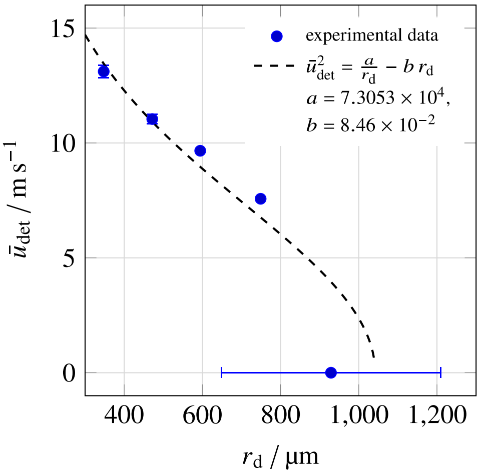

Fig. 15. Measured mean detachment velocity $\bar{u}_{\text{det}}$ as a function of droplet radius r_d with fitted model $\bar{u}_{\text{det}}^2 = \frac{a}{r_d} - b\, r_d$.

- Capillary retention force:

$$F_\sigma \sim \sigma L_{\text{eff}}, \quad L_{\text{eff}} \propto r_d \,. \tag{8}$$

Rearranging for $\bar{u}_{\text{det}}$ yields:

$$\bar{u}_{\text{det}}^2 = \frac{a}{r_d} - b\, r_d \,, \tag{9}$$

where a and b are positive constants depending on material and geometric parameters. This relation explains the observed trend. At small droplet radii, drag dominates and $\bar{u}_{\text{det}} \propto r_d^{-1/2}$, while at large radii the increasing gravitational force reduces the required detachment velocity.

The critical radius for zero detachment velocity (gravity-induced detachment) is found by setting $\bar{u}_{\text{det}} = 0$:

$$r_{\text{d,crit}} = \left(\frac{a}{b}\right)^{1/2} . \tag{10}$$

This model captures the transition between drag-dominated and gravity-dominated regimes and matches the experimental observation that a droplet with $r_d \approx 929\,\mu\text{m}$ detaches without any flow.

Figs. 16–18 depict the droplet detachment process. The fiber position is marked by a red crosshair. The droplet detaching from the fiber is overlaid in gray across multiple frames. The frame in which the liquid neck is about to collapse is overlaid in a darker gray.

Fig. 16 shows that, during detachment, the droplet forms a liquid neck between the liquid residue on the fiber and the main droplet. Driven by the flow, the droplet moves progressively away from the fiber and the neck elongates. For a droplet of radius $r_d = 348\,\mu\text{m}$ at a velocity of $13.8\,\text{m}\,\text{s}^{-1}$, the neck length reaches approximately $1.8\,\text{mm}$ before detachment, from which four satellite droplets are formed. A liquid residue remains on the fiber. The positions of the satellite droplets shown in Fig. 16 are indicated by different symbols. The color encodes the velocity of each satellite droplet. Depending on the breakup dynamics of the neck, a satellite droplet can receive a net impulse in different directions. In Fig. 16, the fiber-proximal satellite droplets 1 and 2 are initially accelerated toward the fiber. However, they do not make contact with the fiber or liquid residual on the fiber, are deflected by the crossflow, and subsequently accelerate in the streamwise direction. The satellite droplets 3 and 4, closer to the main droplet, are initially propelled in the direction of flow towards the detached droplet.

For larger droplets with $r_d = 472\,\mu\text{m}$ and $r_d = 594\,\mu\text{m}$, the length of the liquid neck decreases (see Figs. 17–18). Only 2 liquid segments and therefore satellite droplets are formed during the breakup of the liquid bridge. Similar to Figs. 16, 17 and 18 again show satellite droplets

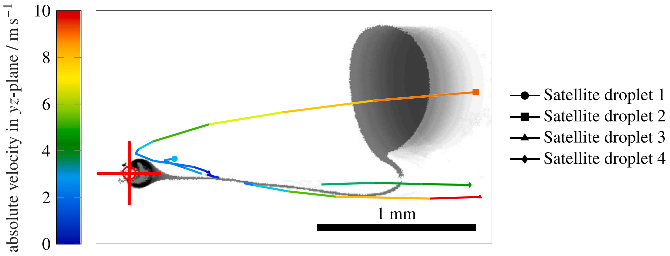

Fig. 16. Detachment of a droplet with $r_{\mathrm{d}} = 348\,\mu\mathrm{m}$ at $\bar{u} = 13.8\,\mathrm{m\,s^{-1}}$ and the trajectories of the generated satellite droplet due to the collapse of the liquid neck.

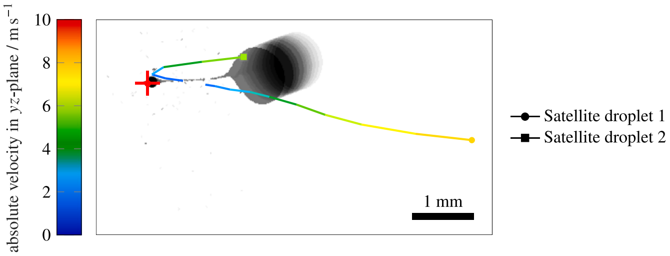

Fig. 17. Detachment of a droplet with $r_{\mathrm{d}} = 472\,\mu\mathrm{m}$ at $\bar{u} = 11.8\,\mathrm{m\,s^{-1}}$ and the trajectories of the generated satellite droplet due to the collapse of the liquid neck.

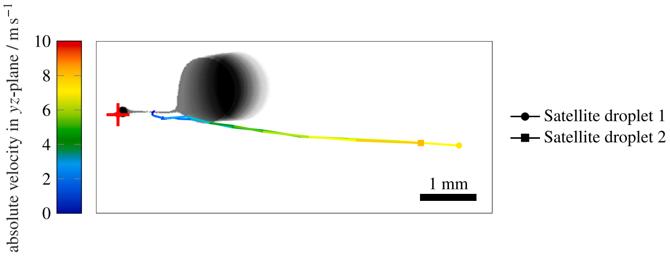

Fig. 18. Detachment of a droplet with $r_{\mathrm{d}} = 594\,\mu\mathrm{m}$ at $\bar{u} = 10.4\,\mathrm{m\,s^{-1}}$ and the trajectories of the generated satellite droplet due to the collapse of the liquid neck.

located closer to the fiber being propelled toward it, while those being created closer to the main droplet are carried initially downstream in flow direction. In Fig. 17, it remains unclear whether satellite droplet 2 eventually coalesces with the main droplet or leaves the focal plane and therefore becomes unobservable.

For the detachment of a droplet with $r_{\mathrm{d}} = 749\,\mu\mathrm{m}$, no satellite droplets could be identified.

It should be noted that for larger droplets, a larger field of view was used in the recordings to capture the entire detachment process. As a consequence, the spatial resolution decreases, and thus the smallest detectable object size shifts from 4 µm to 18 µm. For a meaningful characterization of an object (e.g., determining its shape or boundaries), the object size must be significantly larger than this fundamental resolution limit. In general, as r_{d} increases, the detachment occurs at lower $\bar{u}$, providing less aerodynamic stretching time and force. Hence, the neck remains shorter at collapse and produces fewer fragments.

In comparison to the study by Sahu et al. [10], who reported droplet detachment and aerodynamic breakup on hydrophilic silica fibers at Weber numbers between approximately $2 \leq \mathrm{We} \leq 40$, the present experiments exhibit values in the range of $\mathrm{We} = \frac{\rho_g \bar{u}^2 d}{\sigma} \approx 3.2$ to 5.2, where ρ_g is the gas density. These values correspond to a deformation-dominated regime in which classical bag formation is not expected.

A quantitative interpretation of the absence of the bag–breakup mode can be obtained by considering the dimensionless Ohnesorge number $\mathrm{Oh} = \frac{\mu}{\sqrt{\rho_l\,\sigma\,d}}$, which expresses the ratio of viscous to capillary forces. The present experiments fall into a regime of comparatively high Ohnesorge numbers ($0.5 \leq \mathrm{Oh} \leq 1$), indicating that viscous stresses substantially damp interfacial disturbances and slow down the growth of aerodynamic instabilities. Recent work by Xu et al. [21] has shown that, for increasing Oh, the We-threshold for bag and bag–stamen breakup rises markedly. In other words, viscous droplets require a substantially stronger aerodynamic force to form the thin expanding membrane characteristic of bag breakup.

Table 1
Comparison of experimental conditions and observed detachment processes between Sahu et al. [10] and this work.

Category	Sahu et al. (2013)	This work
Core fiber material	Fused silica	Stainless steel
Fiber coating	Polyamide coating	Perfluoropolyether compound
Wettability	Oleophilic	Oleophobic
initial Droplet Shape	Barrel-shaped	Clamshell-shaped
Fiber diameter	90 µm	80 µm
Fluid	Silicone oil	Hydrocarbon-based synthetic oil
Density ρ_ℓ	930–960 $\mathrm{kg\,m^{-3}}$	870 $\mathrm{kg\,m^{-3}}$
Dynamic viscosity μ	0.01 Pa s–0.1 Pa s	0.13 Pa s
Surface tension σ	20.9 $\mathrm{mN\,m^{-1}}$	31.9 $\mathrm{mN\,m^{-1}}$
Weber number We	2–40	3.2–5.2
Ohnesorge number Oh	0.07–0.8	0.6–0.9
Gas velocity	7.2 $\mathrm{m\,s^{-1}}$–22.7 $\mathrm{m\,s^{-1}}$	1.4 $\mathrm{m\,s^{-1}}$–15.87 $\mathrm{m\,s^{-1}}$
Droplet radius	400 µm–600 µm	276 µm–749 µm
Detachment mechanism		
1. Vibrational breakup		
1.1 without stem and without secondary droplets	✓	✓
1.2 with stem and secondary droplets	✓	✓
1.3 with double stem	✓	✗
2. Double liquid stem	✓	✗
3. Bag-stamen	✓	✗
4. Bag type	✓	✗

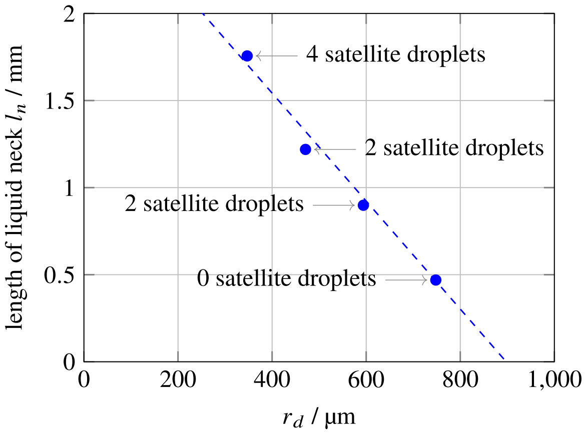

Fig. 19. Length of liquid neck at the moment of detachment.

In the present work, the combination of comparatively large Ohnesorge numbers ($0.5 \leq \mathrm{Oh} \leq 1$), moderate Weber ($3.2 \leq \mathrm{We} \leq 5.2$) numbers and the geometric confinement imposed by the fiber prevents the formation of a freely expanding sheet. As a result, the droplets remain in a deformation-dominated regime and detach by ligament thinning rather than through bag inflation and rupture (see Table 1).

As shown in Fig. 19, an approximately linear relationship is observed between the liquid neck length at the instant of collapse and the size of the detached droplet, given by $l_n = -0.0031 r_d + 2.8$.

Physically, this behavior can be attributed to the higher inertial and viscous forces associated with larger droplet volumes, which accelerate the thinning of the liquid bridge and lead to an earlier pinch-off. Conversely, smaller droplets experience weaker aerodynamic drag and form longer necks before rupture, reflecting a stronger capillary stabilization relative to inertia. A similar trend was reported by Sahu et al. [10], who observed that with increasing droplet size or Weber number, the liquid bridge connecting the droplet to the fiber became progressively shorter before breakup.

The observed decrease in the number of satellite droplets with increasing droplet radius can be interpreted more quantitatively in terms of the competition between Rayleigh–Plateau instability, viscous dissipation, and the available stretching time of the liquid neck. A fully quantitative analysis of the breakup process in terms of Rayleigh–Plateau instability is challenging in the present experiments. While the formation and elongation of the liquid neck can be clearly observed, the instantaneous local neck radius is not resolved with sufficient spatial accuracy to reliably determine the characteristic ligament radius governing the instability. As a result, key quantities such as the most unstable wavelength and its growth rate cannot be evaluated quantitatively with confidence. The following discussion therefore focuses on qualitative trends and scaling arguments, which provide physical insight into the observed dependence of satellite droplet formation on the initial droplet size.

As shown in Fig. 19, the axial neck length at the instant of rupture, l_n, decreases approximately linearly with increasing r_d. Classical linear stability theory [22] for a cylindrical ligament of radius R predicts that the fastest growing Rayleigh–Plateau mode has a wavelength of

$$\lambda_\mathrm{RP} \approx 9.01\,R.$$

The number of unstable wavelengths that can, in principle, develop along the ligament is therefore of the order

$$N_\mathrm{eff} \sim \frac{l_n}{\lambda_\mathrm{RP}} \sim \frac{l_n}{9.01\,R}.$$

Even though the local neck radius R is not resolved with sufficient accuracy to evaluate N_eff quantitatively, the measured decrease of l_n with increasing r_d implies that N_eff must diminish for larger droplets. This provides a natural explanation for the experimentally observed trend. Small droplets form longer ligaments with $N_\mathrm{eff} \gtrsim \mathcal{O}(1)$, which can accommodate several unstable undulations and thus multiple satellite droplets, whereas large droplets form short bridges with N_eff closer to unity, favoring breakup through a single dominant constriction and the formation of at most one or a few satellites.

Viscosity further reduces the growth rate of Rayleigh–Plateau modes. In the present experiments with $0.5 \leq \mathrm{Oh} \leq 1$ is well above the classical transition threshold $Oh \approx 0.1$ at which viscous stresses begin to dominate the instability dynamics. In this viscosity-dominated regime, the growth rate of the most unstable mode scales according to Eggers & Villermaux [23] approximately as

$$\omega \sim \frac{\sigma}{\mu R},$$

while higher-order modes with shorter wavelengths are even more strongly damped. Thus, even in cases where geometric considerations would allow several Rayleigh–Plateau wavelengths along the ligament, viscous dissipation reduces the growth of secondary modes further.

A third contributing factor is the reduced aerodynamic forcing experienced by larger droplets. As shown in Fig. 15, the detachment velocity $\bar{u}_\mathrm{det}$ decreases with increasing r_d. Consequently, the ligament formed by large droplets is exposed to weaker crossflow and is stretched for a shorter time, so it does not evolve into the long, slender configurations that promote multi-wave breakup in smaller droplets.

4. Conclusion

This work has experimentally investigated the dynamics of single oil droplets on horizontally mounted oleophobic fibers exposed to a transverse gas stream. The droplets consisted of a commonly used compressor lubricant. By employing high-speed imaging and quantitative image analysis, the oscillatory motion, deformation, and detachment of droplets were characterized with high temporal resolution. The experiments reveal that, due to the crossflow, droplets undergo oscillatory motion around the fiber, with droplet frequencies increasing as droplet size decreases and gas velocity rises. The measured oscillation frequencies of a droplet of $r_\mathrm{d} = 276\,\mu\mathrm{m}$ reached values of up to 160 Hz. Immediately before detachment, a pronounced reduction in oscillation frequency was observed, caused by strong elongation of the droplet in the flow direction.

The critical gas velocity required for droplet detachment was found to decrease with increasing droplet size, in agreement with theoretical scaling relations based on a balance of aerodynamic drag, gravitational force and capillary adhesion. During the detachment process, the liquid neck forms between the droplet and the fiber, elongates, and eventually pinches off into a small number of satellite droplets. The number of satellite droplets decreases with increasing droplet size.

The Weber numbers achieved in this study (3.2–5.2) correspond to the deformation-dominated regime commonly encountered in coalescence filtration, where droplets typically reach sub-millimeter to millimeter sizes and experience local gas velocities of up to several meters per second. The experimentally observed detachment mechanism of ligament thinning, the formation of a small number of satellites, and viscously moderated pinch-off is therefore directly relevant for predicting droplet removal in technical coalescers.

5. Outlook

Previous investigations by the author have focused on the detachment of droplets from mechanically excited fibers, where periodic vibration of the substrate promotes droplet elongation and breakup. Building upon these findings, the next step will be to combine the aspects of aerodynamic forcing by gas crossflow and mechanical excitation of the fiber. Such experiments will enable a systematic investigation of the coupled effects of external flow and substrate vibration on droplet motion, oscillation, and detachment. Ultimately, the insights gained may support the design of separation devices that are exploited to vibrations.

Beyond the combination of aerodynamic forcing and mechanical excitation proposed, several additional research directions arise from the findings of this study.

Advancing numerical modeling to complement the experiments would enable resolving interfacial stresses, internal flow fields, and instability growth rates that are challenging to access experimentally. Simulations of fiber-supported droplets could help explore parameter ranges beyond those attainable in the laboratory and further elucidate the transition between ligament thinning, satellite formation, and full aerodynamic breakup.

Experiments with multiple droplets deposited on the same fiber and experiments with oil mist separation on individual fibers. In real filtration and mist–coalescence applications, droplets interact through capillary bridges and flow-induced motion, leading to coalescence and hierarchical growth. Investigating how crossflow modifies droplet–droplet interactions, coalescence pathways, and collective detachment dynamics would substantially deepen the mechanistic understanding of droplet-laden fibers.

As an intermediate step toward understanding droplet behavior in densely packed fiber filters, future work could also consider optically accessible, low-density random fiber structures. Such open fibrous networks preserve the essential geometric complexity of real filters with multiple fiber orientations and the possibility of multi-fiber attachment, while still allowing high-speed optical access to individual droplets and ligaments. Studying droplet deposition, coalescence, migration, and detachment in these simplified open multi-fiber structures would help bridge the gap between the controlled single-fiber experiments presented here and the far more complex interactions occurring in practical coalescence filters.

CRediT authorship contribution statement

Alexander Schwarzwälder: Writing – original draft. **Jörg Meyer:** Writing – review & editing. **Achim Dittler:** Writing – review & editing.

Declaration of competing interest

The authors declare that they have no known competing financial interests or personal relationships that could have appeared to influence the work reported in this paper.

Acknowledgment

This work was financially supported by the Deutsche Forschungsgemeinschaft (DFG), Germany as part of project 499469405.

Data availability

Data will be made available on request.

References

[1] R. Mead-Hunter, A.J. King, B.J. Mullins, Aerosol-mist coalescing filters – A review, Sep. Purif. Technol. 133 (2014) http://dx.doi.org/10.1016/j.seppur.2014.06.057.

[2] N.M. Farhan, H. Aziz, H.V. Tafreshi, Simple method for measuring intrinsic contact angle of a fiber with liquids, Exp. Fluids 60 (5) (2019) http://dx.doi.org/10.1007/s00348-019-2733-2.

[3] M.M. Amrei, M. Davoudi, G.G. Chase, H.V. Tafreshi, Effects of roughness on droplet apparent contact angles on a fiber, Sep. Purif. Technol. 180 (2017) 107–113, http://dx.doi.org/10.1016/j.seppur.2017.02.049.

[4] M. Davoudi, M.M. Amrei, H.V. Tafreshi, G.G. Chase, Measurement of inflection angle and correlation of shape factor of barrel-shaped droplets on horizontal fibers, Sep. Purif. Technol. 204 (2018) 127–132, http://dx.doi.org/10.1016/j.seppur.2018.04.033.

[5] A. Bick, F. Boulogne, A. Sauret, H.A. Stone, Tunable transport of drops on a vibrating inclined fiber, Appl. Phys. Lett. 107 (18) (2015) http://dx.doi.org/10.1063/1.4935251.

[6] P. Zhu, W. Wang, X. Chen, F. Lin, X. Wei, C. Ji, J. Zou, Experimental study of drop impact on a thin fiber, Phys. Fluids 31 (10) (2019) http://dx.doi.org/10.1063/1.5116845.

[7] L. Feng, Y. Jiang, C. Machado, W. Choi, N.A. Patankar, K.-C. Park, Directional Self-Propelled Transport of Coalesced Droplets on a Superhydrophilic Cylindrical Wire, Tech. Rep., Northwestern University, 2022.

[8] M.M. Amrei, D.G. Venkateshan, N. D'Souza, J. Atulasimha, H.V. Tafreshi, Novel approach to measuring the droplet detachment force from fibers, Langmuir 32 (50) (2016) 13333–13339, http://dx.doi.org/10.1021/acs.langmuir.6b03198.

[9] B.J. Mullins, A. Pfrang, R.D. Braddock, T. Schimmel, G. Kasper, Detachment of liquid droplets from fibres—Experimental and theoretical evaluation of detachment force due to interfacial tension effects, J. Colloid Interface Sci. 312 (2) (2007) http://dx.doi.org/10.1016/j.jcis.2007.03.051.

[10] R.P. Sahu, S. Sinha-Ray, A.L. Yarin, B. Pourdeyhimi, Blowing drops off a filament, Soft Matter 9 (26) (2013) 6053, http://dx.doi.org/10.1039/c3sm50618e.

[11] H.B. Eral, J. De Ruiter, R. De Ruiter, J.M. Oh, C. Semprebon, M. Brinkmann, F. Mugele, Drops on functional fibers: From barrels to clamshells and back, Soft Matter 7 (11) (2011) 5138–5143, http://dx.doi.org/10.1039/c0sm01403f.

[12] Y. Sun, K.G. Kornev, Does the contact angle hysteresis control the droplet shapes on cylindrical fibers? Colloids Surfaces A: Physicochem. Eng. Asp. 668 (2023) http://dx.doi.org/10.1016/j.colsurfa.2023.131435.

[13] N.M. Farhan, H.V. Tafreshi, Using magnetic field to measure detachment force between a nonmagnetic droplet and fibers, Langmuir (2019) http://dx.doi.org/10.1021/acs.langmuir.9b01313.

[14] B.J. Mullins, R.D. Braddock, I.E. Agranovski, R.A. Cropp, R.A. O'Leary, Observation and modelling of clamshell droplets on vertical fibres subjected to gravitational and drag forces, J. Colloid Interface Sci. 284 (1) (2005) http://dx.doi.org/10.1016/j.jcis.2004.10.013.

[15] B.J. Mullins, R.D. Braddock, I.E. Agranovski, R.A. Cropp, Observation and modelling of barrel droplets on vertical fibres subjected to gravitational and drag forces, J. Colloid Interface Sci. 300 (2) (2006) 704–712, http://dx.doi.org/10.1016/j.jcis.2006.02.059.

[16] C.J. Hotz, R. Mead-Hunter, T. Becker, A.J. King, S. Wurster, G. Kasper, B.J. Mullins, Detachment of droplets from cylinders in flow using an experimental analogue, J. Fluid Mech. 771 (2015) 327–340, http://dx.doi.org/10.1017/jfm.2015.177.

[17] N. Ojaghlou, H.V. Tafreshi, D. Bratko, A. Luzar, Dynamical insights into the mechanism of a droplet detachment from a fiber, Soft Matter 14 (44) (2018) 8924–8934, http://dx.doi.org/10.1039/C8SM01257A.

[18] H. Aziz, N.M. Farhan, H. Vahedi Tafreshi, Effects of fiber wettability and size on droplet detachment residue, Exp. Fluids 59 (7) (2018) http://dx.doi.org/10.1007/s00348-018-2579-z.

[19] N.M. Farhan, H. Vahedi Tafreshi, Universal expression for droplet-fiber detachment force, J. Appl. Phys. 124 (7) (2018) http://dx.doi.org/10.1063/1.5032106.

[20] F. Freese, A. Schwarzwälder, U. Janoske, A. Dittler, Transition from clamshell to barrel shaped oil droplets on a single oleophobic fiber through periodic mechanical excitation, Sep. Purif. Technol. 376 (2025) 133834, http://dx.doi.org/10.1016/j.seppur.2025.133834.

[21] Z. Xu, J. Liu, H. Zhang, T. Wang, Z. Che, Aerodynamic breakup of emulsion droplets in airflow, Droplet 3 (4) (2024) http://dx.doi.org/10.1002/dro2.146.

[22] L.H. Carnevale, P. Deuar, Z. Che, P.E. Theodorakis, Liquid thread breakup and the formation of satellite droplets, Phys. Fluids 35 (7) (2023) http://dx.doi.org/10.1063/5.0157752.

[23] J. Eggers, E. Villermaux, Physics of liquid jets, Rep. Progr. Phys. 71 (3) (2008) http://dx.doi.org/10.1088/0034-4885/71/3/036601.